Draft version March 9, 2017
Preprint typeset using LaTeX style emulateapj v. 12/16/11

arXiv:1703.02700v1 [astro-ph.GA] 8 Mar 2017

EFFECTS OF PRE-IONISATION IN RADIATIVE SHOCKS II: APPLICATION TO THE HERBIG-HARO OBJECTS

Michael A. Dopita [1], Ralph S. Sutherland [1]

Draft version March 9, 2017

ABSTRACT

In an earlier paper we treated the pre-ionisation problem in shocks over the velocity range $20 < v_s < 1000\,\mathrm{km/s}$ in a fully self-consistent manner. Here we investigate in detail the effect of the upstream UV photon field generated in the radiative zone of shocks in the range in which hydrogen is only partly ionised ($20 < v_s < 150\,\mathrm{km/s}$). We show that, as a result of super-heating in the non-equilibrium pre-shock plasma, both the magnetic parameter and the Mach number of the shock is strongly affected by the pre-ionisation state of the gas which controls to a large extent the radiative spectrum of the shock. We use these models to provide specific line diagnostics for Herbig-Haro objects which allow us to solve for both the pre-shock density and shock velocity, and present detailed models of the HH34 jet which allows us to derive the shock conditions, mass-loss rate, momentum flux and chemical abundances in the jet. We show that the refractory elements, Mg, Ca, Fe and Ni are enhanced by 0.22 dex over the solar values, which provides interesting clues about the jet launching mechanism in pre-main sequence evolution.

Subject headings: physical data and processes: atomic data, atomic processes, radiation transfer, shock waves

1. INTRODUCTION

The structure and predicted emission line spectrum of radiative atomic J-shocks is critically dependent on the ionisation state and the magnetic pressure of the gas entering the shock. For fast shocks (Dopita & Sutherland 1996; Allen et al. 2008), the ionisation of this gas is entirely determined by the EUV photons produced in the cooling zone of the shock, which run ahead to fully pre-ionise the hydrogen in the incoming medium. For shocks with velocities $v_s \gtrsim 150\,\mathrm{km/s}$, we can approximate the ionisation state and temperature of the gas entering the shock by an equilibrium photoionisation computation using the upstream EUV photon field.

This approximation breaks down at lower velocities when the upstream photon flux is insufficient to provide full pre-ionisation. In this regime, a useful parameter to describe the pre-ionisation is the *shock–precursor* parameter, Ψ , introduced by Shull & McKee (1979). This is related to the dimensionless ionisation parameter $\mathcal{U}$ commonly used in photoionisation modelling, which is the ratio of the number density of ionising photons to the atom density. This can be also written as $\mathcal{U} = \mathcal{Q}/c$, where $\mathcal{Q}$ is the ionisation parameter in terms of the ratio of ionising photons $\mathrm{cm^{-2}s^{-1}}$ to the particle density ($\mathrm{cm^3}$). To first order $\mathcal{Q}$ can be thought of as the velocity of an ionisation front that would be driven into a neutral medium by an ionising radiation field. We can compare this ionisation parameter in the upstream radiation field generated by the shock to the shock velocity v_s to form the dimensionless shock–precursor parameter:

$$\Psi = \mathcal{Q}/v_s = \mathcal{U}(c/v_s)\,. \quad (1)$$

When $\Psi < 1$, the shock velocity is greater than the velocity of the precursor ionisation front. The photons are trapped by the flux of incoming neutral particles, and there is only a finite time for ionisation and recombination between the moment when the particles enter the precursor region and when they enter the shock. Since the precursor partly-ionised zone in slow shocks is relatively thin, the timescale for incoming atoms to be advected through this zone can be considered short compared to the recombination timescale. In this case, to a good approximation, we can simply balance the upstream EUV photon flux with the number of ionised hydrogen atoms advected into the shock, $xn_{\mathrm{H}}v_s$, where x, is the fractional ionisation of hydrogen in the gas entering the shock. Thus, to a good approximation, $\Psi \sim x$.

In the first paper of this series (Sutherland & Dopita, 2017; hereinafter Paper I), we provided a fully self-consistent modelling of both the pre-shock ionisation and heating over the full velocity range covered by non-relativistic radiative atomic J-shocks, and we investigated how the pre-shock ionisation is influenced by the transverse magnetic field. For the slower shocks which are unable to establish an equilibrium photoionisation region ahead of the shock, we identified three distinct shock regimes:

- *Cold Neutral Precursors* ($v_s \lesssim 40\,\mathrm{km/s}$). Here the upstream precursor radiation field is both too weak and too soft, to either heat or ionise the gas entering the shock front.

- *Warm Neutral Precursors* ($40 \lesssim v_s \lesssim 80\,\mathrm{km/s}$). Here the precursor radiation field contains enough high energy photons, at a very low ionisation parameter, to produce energetic electrons which can heat the gas significantly. While the total ionisation remains fairly low, the heating per ionisation rises, and this heating is not balanced by efficient electron collisional cooling, so the electron temperature can rise to well over 10^4 K.

[1] Research School of Astronomy and Astrophysics, Australian National University, Cotter Road, Weston Creek, ACT 2611, Australia

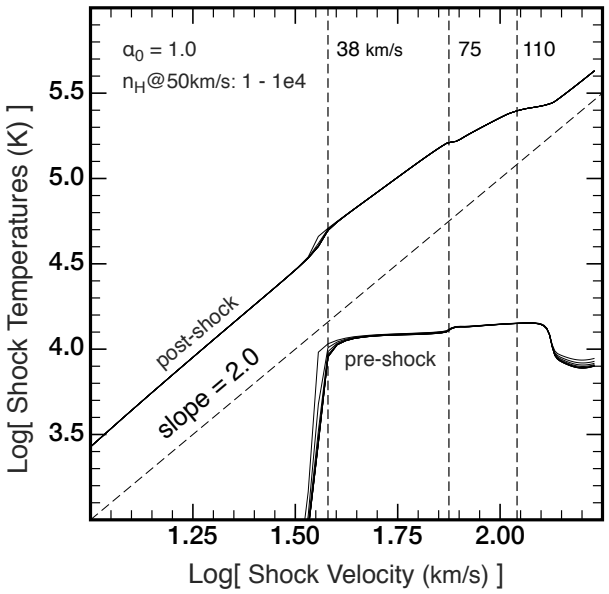

FIG. 1.— The pre- and post-shock temperatures as a function of shock velocity. The different curves correspond to different pre-shock densities ($1 \leqslant n_{\rm H} \leqslant 10000{\rm cm}^{-3}$). These are virtually degenerate. The deviations of the post-shock temperature with velocity from the slope = 2.0 (shown as a dashed line) are fundamentally driven by changes in the molecular weight of the pre-shock plasma. The exception is at around $v_s \sim 38$km/s, where the sudden increase in the pre-shock temperature changes the Mach number of the shock.

- *Warm Partly-Ionised Precursors* ($80 \lesssim v_s \lesssim 140\,{\rm km/s}$). Here $\Psi < 1.0$, so hydrogen is partially pre-ionised. However, hydrogen remains less ionised when entering the shock than would be the case if the gas had time to come into equilibrium with the precursor field.

These three regimes can be readily identified if we consider the pre- and post-shock temperatures as a function of velocity, as shown in Figure 1. Note that the post-shock temperature overall has a slope of +2, but deviates from this due mostly to changes in the pre-shock molecular weight. Note also that the pre-shock temperature in the warm, partly-ionised shock precursor regime is higher than in fast shock regime($v_s > 120\,{\rm km/s}$) as a result of superheating of the gas in the precursor.

In the Herbig-Haro (HH) objects, which are shocks generated by outflows in pre-main sequence stars such as T Tauri and FU Orionis stars, we find examples covering all of these three regimes. Thus, for the HH objects, the issue of pre-ionisation is critical in the interpretation of their spectra. In this paper, we will examine in more detail the role of shock pre-ionisation in controlling the emission line spectrum of HH objects, and will endeavour to define diagnostic tools which can aid both in the interpretation of spectra, and the derivation of the physical parameters.

2. THE HERBIG-HARO (HH) OBJECTS

A quantitative interpretation of the spectroscopy of the Herbig-Haro (HH) objects is capable of providing great insights into the formation, mass accretion and mass ejection by pre-Main Sequence stars. Many of their spectroscopic and dynamical properties have been summarised in a series of excellent reviews (Schwartz 1983; Edwards et al. 1993; Reipurth & Cernicharo 1995; Reipurth & Heathcote 1997; Bohm & Goodson 1997; Reipurth & Bally 2001; Bally & Reipurth 2002)

Since Schwartz (1975) recognised that the HH objects are shock excited, there have been many attempts to explain their spectra using both radiative shock modelling (Dopita 1978; Böhm et al. 1980; Dopita et al. 1982a, 1987; Raga 1995; Raga et al. 1996) and hydrodynamic modelling (Hartmann & Raymond 1984; Raga & Bohm 1985; Hartigan et al. 1987; Biro & Raga 1994; Henney 1996).

As first pointed out by Dopita et al. (1982b), the HH shocks arise in a dense, two-sided jet thrown out by an eruptive low-mass pre-main sequence star. These jets may extend over parsec scales (Heathcote et al. 1998; Bally & Reipurth 2002; Bally et al. 2002a) and can interact with the surrounding ISM in a variety of ways. In some objects dense "bullets" of gas are episodically ejected, producing fast bow-shocks and slower cloud shocks. In others, the shocks are produced as weak internal jet shocks, which generally have low internal shock velocities and correspondingly low excitation, but which display very rapid transverse velocities (Bally et al. 2002a; Hartigan et al. 2005; Beck et al. 2007; Raga et al. 2016).

The HH objects display a wide range of excitation ranging from the extremely low-excitation objects described by Böhm et al. (1980), through the rich spectrum displayed by objects such as HH1 (Solf et al. 1988), up to extremely high excitation objects such as HH80 and 81 (Heathcote et al. 1998), which have spectra which are indistinguishable from the fast radiative shocks found in supernova remnants. Generally, the [S II] ratios indicate that the pre-shock densities are high, and the strength of the [Fe II] lines as well as of the Ca II] and Mg I] lines (Raga et al. 1996; Reipurth et al. 2000) indicates that dust has largely been destroyed in the shock (Beck-Winchatz et al. 1996). The (then) available optical spectrophotometry on the HH objects was reviewed by Raga et al. (1996).

The low-excitation HH objects present a particularly interesting optical spectrum. In these, lines such as [C I] $\lambda\lambda 9823, 9849$ can exceed the strength of Hα, as can [O I] $\lambda 6300$, while [N I] $\lambda\lambda 5198, 5200$ can exceed Hβ in intensity. In addition, these objects display a large Hα/Hβ ratio, the absolute surface brightness of Hβ is low, and the 2-photon continuum of hydrogen can become relatively very strong (Böhm et al. 1980; Dopita et al. 1982a). Such properties can only be explained in terms of low-velocity shocks with a low pre-ionisation fraction of hydrogen. In the following sections, we will examine how our new self-consistent models can inform us about the physical conditions prevailing in such objects.

3. SHOCK DIAGNOSTICS FOR HH OBJECTS

It should be noted at the outset that shock models adopting a single shock velocity and pre-shock density will fail to reproduce the observed spectra of HH objects. This is because ground-based spectrophotometry includes a wide range of shock conditions within the aperture used for the observation. We may recognise the presence of a wide number of shock types. These include

bow shocks (Raga & Bohm 1985; Hartigan et al. 1987; Henney 1996) and cocoon shocks (Heathcote et al. 1998) propagating in the surrounding ISM, in addition we may find cloud shocks, jet termination shocks and working surface shocks internal to the jet (Raga 1995; Reipurth & Heathcote 1997; Bally & Reipurth 2002; Beck et al. 2007). To separate these requires high spatial resolution integral field spectrophotometry of which, apart from the studies by Beck et al. (2007) and López et al. (2010), there has been very little.

3.1. *Model Grid*

To provide a set of shock models which can be used to derive shock diagnostics for the physical conditions prevailing in HH objects, we have run a dedicated series of models using Local Galactic Concordance (LGC) abundances (Nicholls et al. 2016, MNRAS, in press), and covering the velocity range $15 \leqslant V_s \leqslant 150$km/s, in steps of 2.5 km/s at fixed shock ram pressure. This eliminates the primary velocity-dependence of the surface brightness, and is more applicable to real objects in which the pressure is the key parameter which drives shocks of varying velocity through a multiphase medium, or in the case of a cloud driving into the ISM, which produces a fast bow shock and a slower cloud shock with common ram pressure.

Given that Beck-Winchatz et al. (1996) finds that, in most HH objects, the Fe abundances seem to be un-depleted in the gas phase, as our primary HH grid we adopted dust-free models. We have also run a depleted set with [Fe/H] = -1.0, where the appropriate depletion factors for the individual refractory elements are taken into account, as described in Dopita et al. (2016). However, these models do not provide a good fit to the observed HH object spectra. The ram pressure, $P = \rho V_s^2$ is normalised to the pre-shock hydrogen number density at a shock velocity of 50 km/s. For a pre-shock hydrogen density $n_1 = 1.0\,\mathrm{cm}^{-3}$, this corresponds to a pressure $\log P = -10.27$ dynes cm^{-2}. Constant pressure shock families in the range $15 \leqslant V_s \leqslant 150$km/s were run for the pre-shock hydrogen densities of $n_\mathrm{H} = 1, 3, 10, 30, 300, 1000, 3000$ and 10000 cm^{-3}.

As for the magnetic field, we have assumed that equipartition between the magnetic and the gas pressures pertains in the proto-ionised state, and that both the particle density and the magnetic field remain constant in the pre-ionised region. Thus, in these models, the magnetic field no longer dominates the gas pressure when the pre-ionised gas has been preheated. The main effect of the magnetic field is to limit the compression in the cooling zone of the shock (see Paper I), which affects [O II] and [S II], but has little effect on other line ratios in our computed velocity range. This effect was clearly shown by Hartigan et al. (1994).

3.2. *Shock Surface Brightness*

The key factor in determining the observability of a shock is clearly its surface brightness. In Figure 2 we show the Hβ surface brightness as a function of both ram pressure and shock velocity. Naively, we might expect the Hβ surface brightness to scale as the rate of mechanical energy flux across the shock $\dot{E} = 0.5\rho v_s^3$. This is clearly not the case. In practice, it is the product of the number of recombinations occurring per hydrogen atom entering the shock and the rate at which these atoms are processed through the shock which governs the surface brightness. This is a more complex function, but which scales more closely as the ram pressure, ρv_s^2. For slow shocks, the surface brightness falls rapidly due to the rapidly decreasing mean fractional ionisation of hydrogen within the shock. As a consequence shocks with velocities $v_s \lesssim 30$ km/s are unlikely to be observed. This concurs with the observations of Böhm et al. (1980), who found that the lowest excitation HH objects do indeed have the lowest surface brightness. Figure 2 shows an increase in surface brightness occurs once the pre-shock gas becomes becomes warm at $v_s \gtrsim 38$ km/s, followed by a decrease once the pre-ionisation fraction becomes appreciable at $v_s \gtrsim 75$ km/s, due to the changing mean atomic weight, μ. At the highest velocities, the surface brightness starts to approach our expectation.

3.3. *Precursor Surface Brightness*

While the degree of pre-ionisation remains low, for shock velocities $v_s < 75$ km/s, the precursor has a very low surface brightness compared with the shock and remains essentially unobservable. To be seen in the low velocity regime, the shock would have to be externally irradiated by a UV source. Such shocks were first identified by Bally & Reipurth (2001), and have since been extensively studied both observationally (Bally et al. 2002b; Bally 2009; Comerón et al. 2013; Riaz & Whelan 2015) and theoretically (Kajdič & Raga 2007). However, the models presented here are not appropriate for such objects.

At higher velocities, the precursor emission becomes more significant relative to the optical emission in the main shock, and finally, when the shock is fast enough to supply soft X-rays to the precursor region ($v_s \gtrsim 250$ km/s) the precursor emission is sufficient to profoundly influence the global shock + precursor spectrum (Dopita & Sutherland 1995).

In Figure 3 we show the surface brightness of the precursor in the range of velocities relevant to the HH objects. This should be compare with the surface brightness of the shocks given above in Figure 2. In the regime where the precursor is cold, and essentially unionised, the contribution of the precursor can be entirely neglected. Even at the upper limit of the HH grid ($v_s = 150$ km/s), the brightness of the precursor only amounts to a few percent of the brightness of the radiative shock, and so remains rather difficult to observe.

3.4. *Balmer Decrement and Hydrogen 2q Emission*

Dopita et al. (1982a) discovered that many low-excitation HH objects show a pronounced enhancement of the hydrogen two-photon (2q) continuum, accompanied by an increase in the intrinsic Hα/Hβ ratio. They explained this in part in terms of slow-shocks moving into a medium with low pre-ionisation of hydrogen. However, their models were limited at F(Hα)/F(Hβ) $\sim$ 3.9 and F(2q)/F(Hβ) $\sim$ 60. To obtain the maximal values observed (F(Hα)/F(Hβ) $\sim$ 4.6 and F(2q)/F(Hβ) $\sim$ 120), (Dopita et al. 1982a) needed to additionally invoke finite-age shocks.

Our current self-consistent steady-flow shock models produce flux ratios which naturally reach these maximal

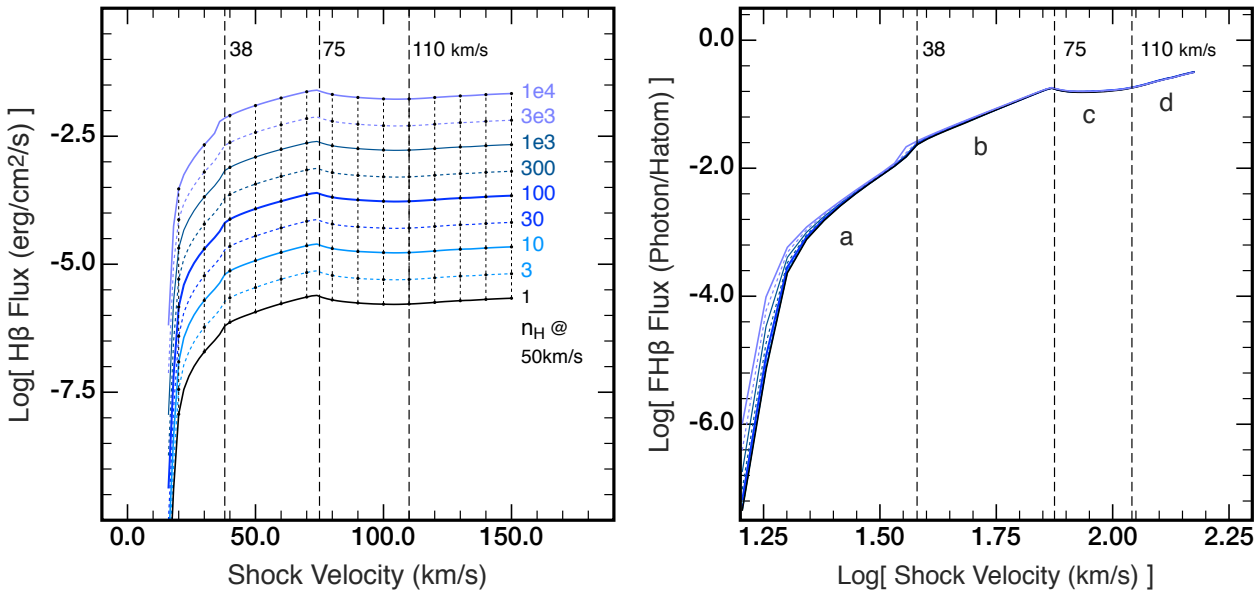

FIG. 2.— (Left) the surface brightness of the radiative shocks as a function of shock velocity and pre-shock hydrogen number density $n_{\rm H}$ in units of cm^{-3}. (Right) As was shown in Paper I, this can be simply scaled as $\Psi_{H\beta}$, the number of Hβ photons produced per hydrogen atom entering (or advected into) the shock, which almost entirely removes the density dependence. The velocity thresholds between the shock types summarised in the introduction are marked as dashed vertical lines, and fits to the segments a–d are given in Paper I.

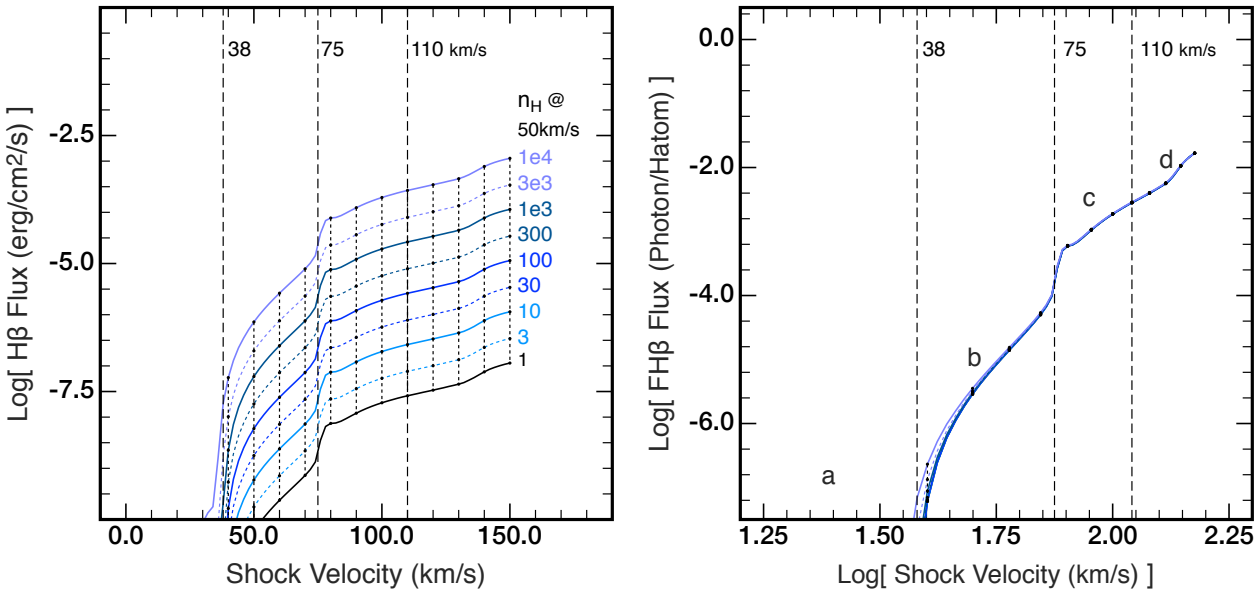

FIG. 3.— As Figure 2 but for the shock precursor. Left: the surface brightness of the precursors as a function of shock velocity and pre-shock hydrogen number density $n_{\rm H}$ in units of cm^{-3}. Right: the number of Hβ photons produced per hydrogen atom entering (or advected into) the shock. The velocity thresholds between the shock types summarised in the introduction are marked as dashed vertical lines.

values observed in HH objects without having appeal to finite age shocks, provided that the shock velocities are very low – of order 15-20 km/s (see Figure 4). Less extreme enhancements of F(2q)/F(Hβ) occur in all shocks with $v_s < 45$ km/s, but all models with less than complete pre-ionisation display enhanced Balmer decrement due to collisional excitation of the Hydrogen $n = 3$ level. If the pressure driving the shock does not vary by too much object to object, Figure 2 also implies that the shock surface brightness should be also correlated with Balmer decrement and the 2q excess, provided that the pressure driving the shock does not vary by too much object to object. This would help explain the correlation noted by Böhm et al. (1980) in their Figure 1.

A different way of producing enhanced Hα/Hβ ratios in HH objects was recently identified in HH1 and 2 by Raga

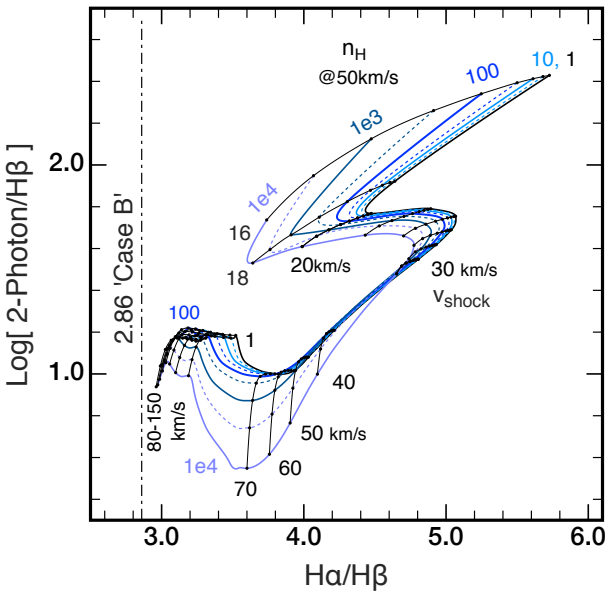

FIG. 4.— (From Paper I) The relationship between the Balmer decrement, Hα/Hβ, and the hydrogen 2-photon continuum. Note that it is possible to obtain an enhancement of the 2-photon continuum by a factor greater than 30. In all shocks, the intrinsic Balmer Decrement is larger than the photoionised nebula Case B value, 2.86 (marked here as a vertical dashed line).

et al. (2015). Using HST imaging, they found strong enhancements in this ratio immediately behind the bow shock of these objects. In this regard, the HH objects are behaving in the same way as the Balmer-dominated shocks seen in supernova remnants. These require that the gas entering the shock has not passed through an ionised precursor (which implies either finite or partially-radiative shocks) resulting in strong collisional excitation of hydrogen in the region where it is first becoming ionised. The theory of such 'collisionless' shocks was originally developed by Chevalier (1978).

3.5. *Velocity Diagnostics*

The observations of HH objects summarised by Raga et al. (1996) display a paradox that has been encountered in all earlier attempts to derive shock parameters, namely, that the strength of the low-excitation lines [O I], [N,I] and [S II] implies very low shock velocities, while the simultaneous presence of higher-excitation lines such as [N II] and [O III] requires higher shock velocities; above 50 km/s in the case of [N II] and above 80 km/s for [O III]. The root cause of this discrepancy appears to be that the HH shocks are - in general - composite, arising from the summation of a jet shock of some kind (internal working surface, jet density pulse or jet Mach disk) and an external bow or cocoon shock of both higher velocity and lower density. For this reason, shock diagnostics which depend on a limited set of line ratios must be treated as indicative, rather than quantitative. Furthermore, much of the spectrophotometry on the HH objects is old, and of limited accuracy by today's standards, and reddening corrections are heterogeneous, depending on the reddening "law" adopted. In addition, reddening corrections are often based upon correcting observed Balmer decrements to the standard Case B decrement, while Section 3.4, above, makes it clear that such an assumption is not generally valid. However, within these caveats, let us proceed regardless to determine what physical parameters we can estimate using the existing data from Raga et al. (1996) and Heathcote et al. (1998).

In principle, the shock velocity could be derived from the observed [N I]λ5200/Hβ or [O I]λ6300/Hα alone. This has been previously done in the extensive grid of shock models by Hartigan et al. (1994), who investigated the effect of high pre-shock magnetic fields as well as high density in HH shocks. In Figure 5, we show the results for our self-consistently pre-ionised and pre-heated set of models. Our models show very little density dependence for the slower shocks. This is driven by the fact that these have very low fractional pre-ionisation, and low maximum ionisation fractions as well, so all slow shock models remain at, or close to, the low density limit. At higher velocities, the agreement with the Hartigan et al. (1994) models seems to be quite good. Our models show evidence for collisional de-excitation in [N I]. By contrast, the [O I]λ6300/Hα ratio is enhanced as a consequence of collisional de-excitation in both [N I] and [S II].

When comparing these two line ratios with the observations of HH objects we find that there is a disagreement between the two, in the sense that the observed [N I]λ5200/Hβ provides a somewhat lower shock velocity than does the [O I]λ6300/Hα ratio. We simply adopt the mean of these two as the estimated shock velocity using these ratios.

Other ratios can also be used to constrain the shock velocity. In Figure 6 we present what appear to be the most useful of these ratios; [O I]λ6300/Hα, [N II]λ6584/[S II]$\lambda\lambda$6717, 6731 and [O III]λ5007//Hβ. In this particular set, all ratios depend only weakly on the assumed reddening correction. In addition, the [O III]λ5007//Hβ ratio is effectively independent of density and the density sensitivities of the [O I]λ6300/Hα and N II]λ6584/[S II]$\lambda\lambda$6717, 6731 ratios are similar.

Due to the issues identified above, the observed [N II]λ6584 line strengths are stronger than predicted in a single-velocity shock model. Another factor which may cause this effect is the fact that many HH objects are embedded in weak diffused ionised nebulosity which is characterised by large [N II]λ6584/Hα line ratios. A good agreement between the observed [O II]λ6300/Hα and the theoretical [N II]λ6584/[S II]$\lambda\lambda$6717, 6731 can be obtained if the latter ratio is enhanced by $\sim$ 0.4 dex. With this estimate of the enhancement, we have also used the observational material from Raga et al. (1996) and Heathcote et al. (1998) to derive shock velocities (ignoring the values given by the [O III]λ5007//Hβ ratio for this exercise).

Finally, in Figure 7 we show the [N I]λ5200/Hβ vs. [O I]λ6300/Hα/[N II]λ6584 ratio, which appears to provide a good velocity discrimination up to a velocity of about 70 km/s, and against which the observational data can be directly compared. Also shown are the spectrophotometric data from Raga et al. (1996) and Heathcote et al. (1998) in which we have applied the 0.4 dex offset to the Nitrogen lines which was estimated above. On the figure, the red points represent those objects with [O III]/Hβ > 0.15, and the blue points the rest. Clearly, those objects showing the [O III] line are of systematically higher velocity than the others, but none are com-

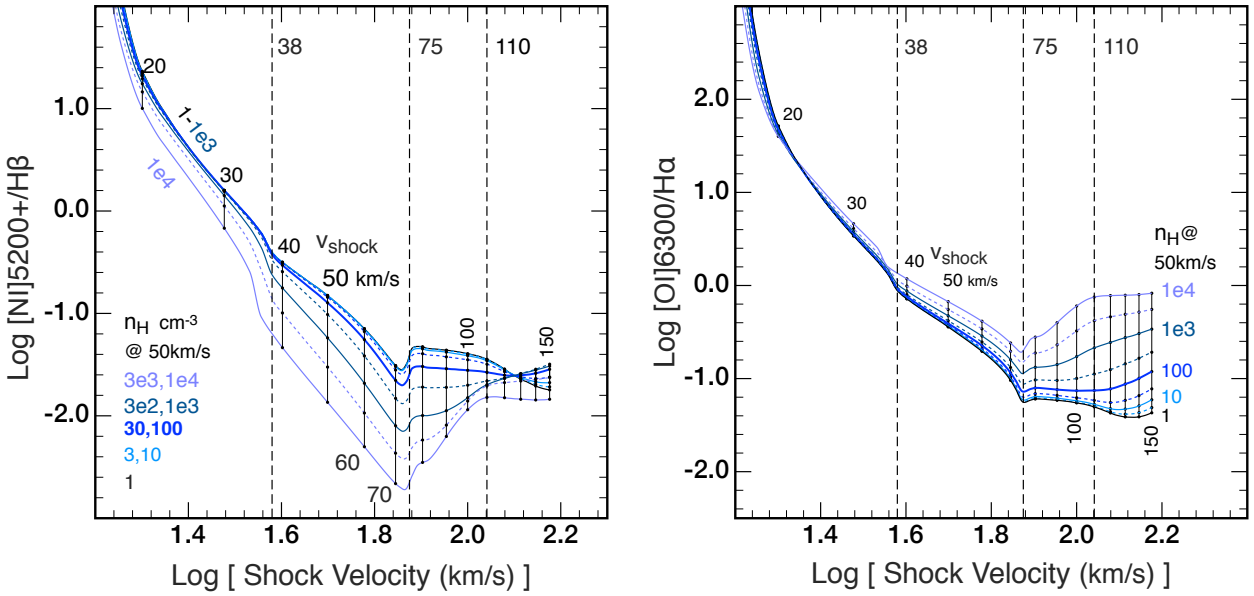

FIG. 5.— The variation of [(left) the N I]λ5200/Hβ and [(right) O I]λ6300/Hα ratios with shock velocity and pre-shock density.

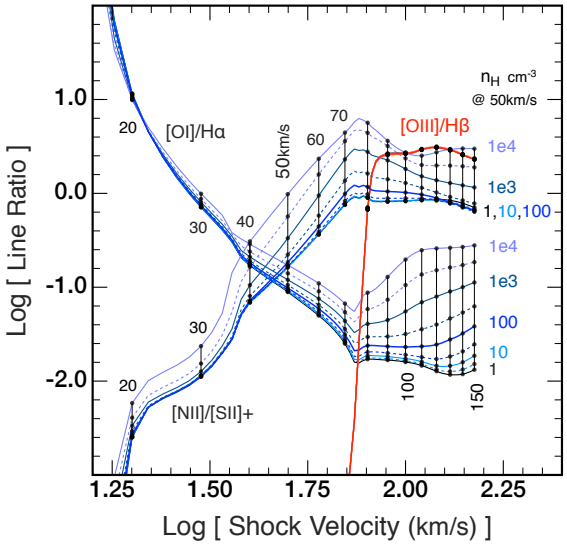

FIG. 6.— Shock velocity diagnostic ratios derived from the [O I]λ6300/Hα, the [N II]λ6584/[S II]λλ6717, 6731 and the [O III]λ5007/Hβ emission line ratios. Note that collisional de-excitation effects and reddening correction effects are partly compensated for by this particular choice of ratios.

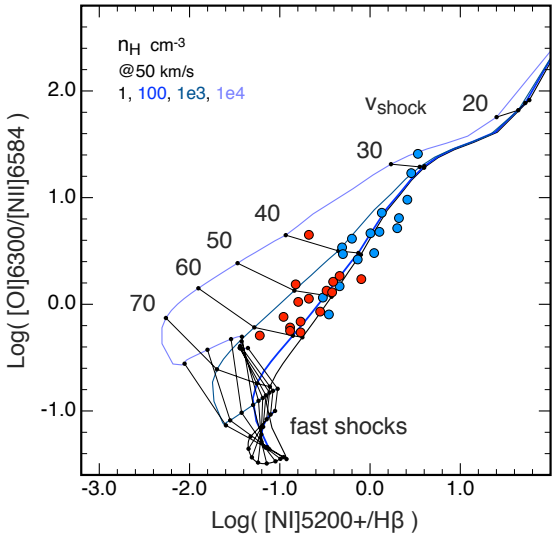

FIG. 7.— A shock velocity diagnostic derived from the [N I]λ5200/Hβ and the [O I]λ6300/Hα/[N II]λ6584 ratios. The red points represent those objects with [O III]/Hβ > 0.15, and the blue points are for objects with slower shock velocities in which the [O III] λ5007 emission is either weak or absent.

patible with the $v_s \sim 80$km/s needed to produce this line in the single shock models. Clearly therefore, the spectrophotometric data of the HH objects must reflect the presence of a fairly wide range of shock velocities present within them.

With this offset we have estimated the velocities in the lower-velocity (cloud) shock component of the observed HH objects given in Raga et al. (1996) and Heathcote et al. (1998). In all those objects for which [O III]λ5007 is detected, the observed [O III]λ5007//Hβ ratios imply (bow) shock velocities of close to 75–85 km/s, while the lower-ionisation lines provide a solution with a lower velocity than this. The exception to this rule is HH81, for which a fairly consistent solution with $70 \lesssim v_s \lesssim 85$ km/s is obtained using all three line ratios. In Table 1 we list the indicative shock velocities so obtained. We emphasise that these are merely crude estimates, and we have no way of evaluating the error on either the data or the fit. These serve merely to inform future attempts to provide detailed models of individual objects.

3.6. *Estimating the Ram Pressure*

In our models, the density-sensitive [S II] ratio λλ6731/6717 serves to provide an estimate of the ram

pressure in the shock. However, this ratio depends not only on the fractional ionisation of the gas entering the shock, but also on the degree of ionisation reached within the shock, and on the compression factor of the gas passing through the cooling region of the shock. To fit the observations to these self-consistent pre-ionisation and pre-heating shock models we need have a means of disentangling the shock velocity from the ram pressure.

One way of doing this is to plot a density sensitive ratio such as [S II] $\lambda\lambda$6731/6717 against a velocity sensitive ratio. Suitable candidate ratios are [N II]λ6584/[S II]$\lambda\lambda$6717, 6731 or the [N II]λ6584/[N I]$\lambda\lambda$5198, 5200. These are shown in Figure 8, along with the observational data from Raga et al. (1996) and Heathcote et al. (1998). Here, again, we distinguish the objects with [O III]/Hβ < 0.15 (in blue) from those with larger [O III]λ5007//Hβ emission line ratios (in red). It is clear from the plot that the objects with larger [O III]/Hβ ratios are indeed characterised by larger shock velocities. Again, some of these points would indicate shock velocities as low as 35 km/s, while shock models do not produce appreciable [O III] emission until the velocity is in excess of 75 km/s. Nonetheless, the agreement of the observed points between panels (a) and (b) of Figure 8 is rather good.

A better way to estimate the ram pressure is to directly use the shock velocity derived above to solve for the ram pressure as indicated by the [S II] ratio $\lambda\lambda$6731/6717 ratio. This is shown in Figure 9. At low shock velocities, the fractional ionisation of hydrogen in the shock remains low, and high pre-shock densities are required to raise the [S II] ratio $\lambda\lambda$6731/6717 ratio above its low density limit. Typical pre-shock densities for the observed HH objects are in the range $10 - 1000\,\mathrm{cm}^{-3}$. The derived velocities, densities and implied ram pressures for individual HH objects are listed in Table 1.

TABLE 1
Estimated global shock parameters of the HH objects using the diagnostics in this paper along with the spectrophotometric compilation of Raga et al. (1996) and Heathcote et al. (1998).

HH Object	$\log(P/k)$ $\mathrm{cm}^{-3}\mathrm{K}$	V_s km/s	$\log(n_1)$ cm^{-3}
[O III]/Hβ < 0.15 :			
HH7	7.44 ± 0.23[1]	29 ± 3	2.32 ± 0.14
HH10	7.53 ± 0.33	31 ± 5	2.35 ± 0.15
HH11	7.22 ± 0.20	33 ± 4	1.99 ± 0.05
HH43B	7.79 ± 0.17	37 ± 3	2.46 ± 0.04
HH43C	7.02 ± 0.30	36 ± 3	1.74 ± 0.06
HH47A	6.63 ± 0.34	36 ± 3	2.19 ± 0.13
HH47C	6.53 ± 0.34	42 ± 3	1.18 ± 0.02
HH111V	7.07 ± 0.33	43 ± 4	1.70 ± 0.02
HH111D-J	7.31 ± 0.15	33 ± 3	2.08 ± 0.05
HH125F	< 5.52	46 ± 7	< 0.0
HH128	7.20 ± 0.017	32 ± 3	2.00 ± 0.02
HH54B	7.03 ± 0.05	42 ± 4	1.57 ± 0.05
HH111L	6.90 ± 0.24	40 ± 3	1.54 ± 0.02
HH83BD	6.98 ± 0.41	45 ± 7	1.48 ± 0.05
HH34MD	5.23 ± 0.10	38 ± 3	0.00 ± 0.03
[O III]/Hβ > 0.15 :			
HH123	7.93 ± 0.12	43 ± 3	2.47 ± 0.03
HH124A-C	6.97 ± 0.28	49 ± 6	1.41 ± 0.08
HH24A	7.58 ± 0.15	45 ± 4	2.08 ± 0.05
HH158	8.19 ± 0.07	55 ± 3	2.50 ± 0.04
HH240	7.35 ± 0.11	43 ± 3	1.89 ± 0.11
HH54C	6.89 ± 0.08	40 ± 4	1.48 ± 0.02
HH234	6.60 ± 0.32	46 ± 6	1.10 ± 0.10
HH56	7.45 ± 0.05	43 ± 3	1.99 ± 0.03
HH3	8.56 ± 0.28	54 ± 4	2.92 ± 0.10
HH43A	7.13 ± 0.23	49 ± 3	1.57 ± 0.05
HH34apex	5.55 ± 0.31	51 ± 4	0.00 ± 0.02
HH1	7.96 ± 0.10	51 ± 3	2.33 ± 0.07
HH2H	8.08 ± 0.07	56 ± 3	2.38 ± 0.02
HH32	7.92 ± 0.14	57 ± 3	2.22 ± 0.06
HH81	8.43 ± 0.22	74 ± 6	2.50 ± 0.04
HH80	7.67 ± 0.05	55 ± 5	2.00 ± 0.02

[1] Errors given are the fitting errors only, and do not include the photometric errors, which are not known..

4. PHYSICAL SCALES

The density of the material being shocked, and the geometry of the shock itself determine the physical extent of the shock and its precursor. Clearly, these parameters determine the applicability of our computed shock models to real HH objects. In the following subsections we provide these essential quantities.

4.1. *Cooling Lengths*

It is useful to investigate the cooling length directly, since this determines the physical extent of the shock structure on the sky. However, at a given shock velocity, provided that collisional de-excitation effects are negligible, the cooling timescale (and therefore the cooling length) of the post-shock plasma varies inversely as the density. Thus the product of the cooling length and the pre-shock density – which we term the cooling column, since it has dimensions of cm^{-2} – provides a quantity which, at the low density limit, is independent of density.

In Paper I, we instigated this quantity over the full range of shock, density, and magnetic field parameter. When hydrogen is fully pre-ionised, for shock velocities above $v_s \sim 110$ km/s, the cooling column can be represented by a single function. However, in the case of the HH objects, the variation in both the degree of pre-ionisation and the pre-shock temperature (which affect both the Mach number of the shock and the electron density at a given shock velocity and pre-shock density) invalidate a general scaling of this nature. In Figure 10, we show both the computed cooling length (D_3; the distance to a final electron temperature of 1000 K) and the cooling column (λ_3; again to a final electron temperature of 1000 K) as a function of both shock velocity and pre-shock density.

The cooling length over the greatest range of interest for the HH objects ($20 < v_s \sim 75$ km/s, actually decreases with shock velocity, thanks to the increased fractional ionisation reached in the shock, resulting in more efficient cooling. A 20 km/s shock with a pre-shock density of $n_\mathrm{H} = 1000\,\mathrm{cm}^{-3}$ has a cooling length of 10^{15} cm. Using an assumed distance to the Orion Nebula Cluster of 400 pc (Kim et al. 2016), this corresponds to an angle of 0.17 arc sec. on the sky, which can just be resolved with HST. Using more typical values for the HH objects given in Table 1 and Fig 8 ($v_s \sim 50$ km/s, $n_\mathrm{H} = 100\,\mathrm{cm}^{-3}$), the corresponding cooling distance is $\sim 1.6 \times 10^{14}$ cm which corresponds to an angle of only

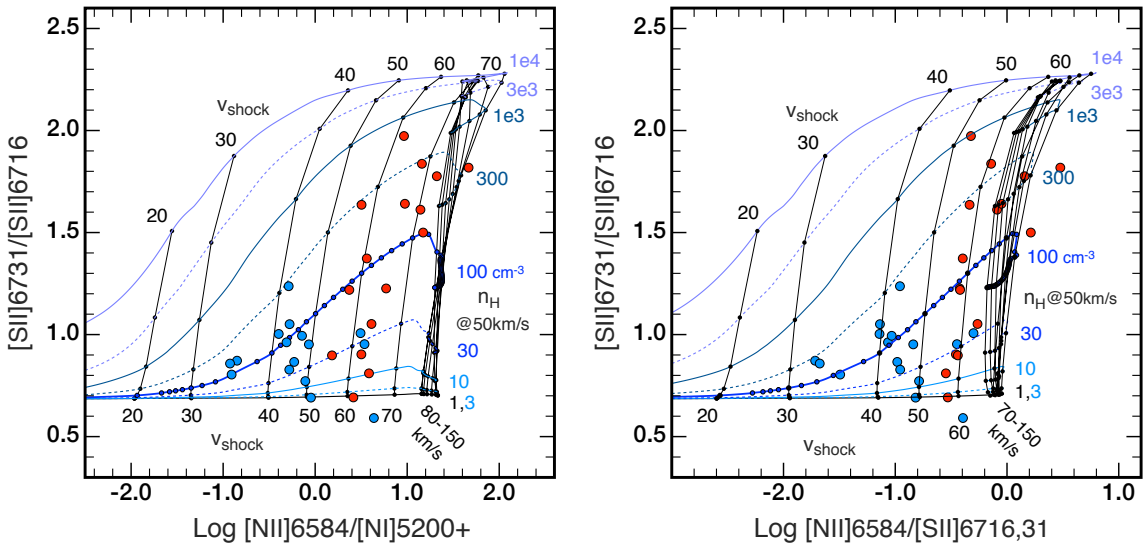

FIG. 8.— Line diagnostics to designed to provide a simultaneous solution for both shock velocity and shock ram pressure for HH objects. The strength of the [N II] line relative to ions of lower ionisation potential is sensitive to the shock velocity below $v_s \sim 80\,$km/s while the [S II] $\lambda\lambda$6731/6717 measures the compression factor in the shock, which is sensitive to the ram pressure (given on the right of each plot in units of dynes cm^{-2}). For convenience, we also give the corresponding pre-shock hydrogen density (cm^{-3}) for a shock velocity of 50 km/s. The observed points are derived from the compilation of Raga et al. (1996), supplemented by the subsequent observations of Heathcote et al. (1998). The blue symbols are for those objects displaying [O III] λ5007 less than 15% of Hβ, and the strong [O III] emitters are in red.

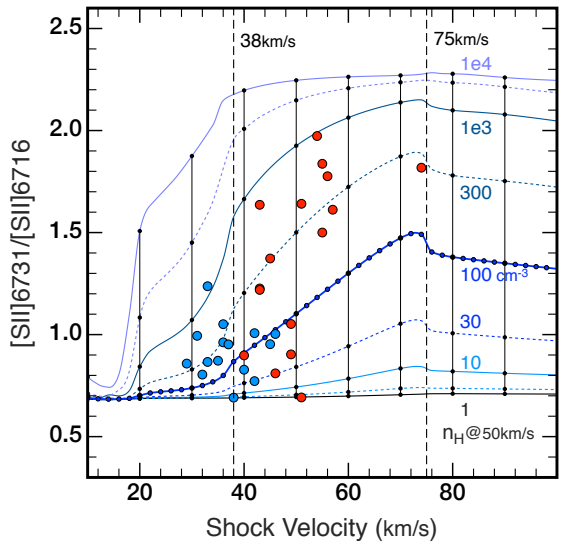

FIG. 9.— The [S II]$\lambda\lambda$6717/6731 line ratio provides a pressure diagnostic, provided that the shock velocity is known. Here we have used Figure 6 to estimate the shock velocity for HH objects compiled by Raga et al. (1996), supplemented by the subsequent observations of Heathcote et al. (1998). The meaning of the symbols is the same as in Figure 8.

0.03 arc sec. on the sky at the distance of Orion.

4.2. *Scale of the Precursor*

For shock velocities below 38 km/s, the precursor is cool, and remains essential un-ionised. In this regime, what few ionising photons exist are absorbed in a column corresponding to the absorption edge opacity of atomic hydrogen ($\sim 10^{17}\,$cm^{-2}). For faster shocks, because the precursor fractional ionisation changes in a continuous manner ahead of the shock, the precursor region cannot be characterised by a single characteristic length. Instead, we choose to give the precursor lengths to initial H-ionisation fractions of 50%, 10%, 1% and 0.1%. These are shown as a function of shock velocity and pre-shock density on the left hand panel of Figure 11. The left panel shows that the full range of possible cooling lengths may vary over 6 or more orders of magnitude from $\sim 10^{13}$ to over 10^{18} cm for shocks faster than $\sim 40\,$km/s. This rather complex panel is greatly simplified when we express the thickness of the precursor in terms of a Hydrogen column density, since this column density is independent of the physical density for any chosen value of the initial H-ionisation fraction (the right hand panel of Figure 11). Using typical values for the HH objects given in Table 1 and Fig 8 ($v_s \sim 50\,$km/s, $n_{\rm H} = 100\,$cm^{-3}), the corresponding spatial scale of the precursor to an initial ionisation fraction of 0.1% is $\sim 3 \times 10^{15}\,$cm which corresponds to an angle of only ~ 0.5 arc sec. on the sky at the distance of Orion. However such a precursor would be very hard to detect.

Note that the degree of ionisation inside the precursor increases relatively slowly as the shock is approached. This is a result of the time-dependent behaviour of the pre-ionisation, and is quite unlitke what would be expected for a precursor in photoionisation equilibrium. As a result, precursors, when visible, would be expected to appear rather "fuzzy" and indistinct. Thus, the concept of a precusor length is rather poorly defined. Faster shocks will produce much stronger and more extensive precursors. In these the internal ionisation is much closer to the photoionisation equilibrium, and for shock velocities above $\sim 150\,$km/s the approximations made by Dopita & Sutherland (1996) are valid.

If we take the 10% ionisation curves from Figure 11 and compare these curves with the scale of the cooling region

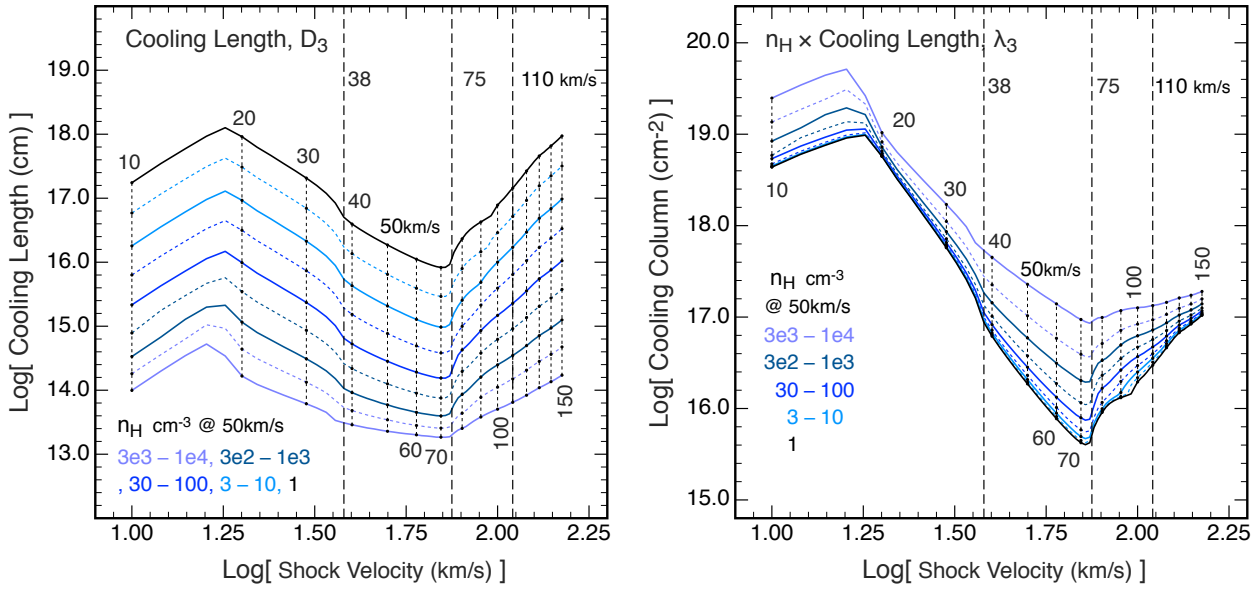

FIG. 10.— The cooling length (D_3), the distance to a final electron temperature of 1000 K) and the cooling column to a final electron temperature of 1000 K (λ_3) as a function of both shock velocity and pre-shock density.

of the shock in Figure 10, we see that the precursor length is always physically larger than the shock cooling length. In practice, this may mean that the precursor ISM runs out before a full precursor structure has developed, which in turn opens up the precursor to irradiation by external UV fields, briefly mentioned above in Section 3.3.

The precursors of plane-parallel shocks computed here give upper limits to the true strength of the precursor, since the upstream diffuse field is maximised in this geometry. In other geometries such as in bow shocks, the diffuse field is strong only at the leading edge, and geometrical dilution effects will reduce the degree of pre-ionisation in the Mach cone. This regime has been modelled in 3-D with ray-tracing methods used for the radiative transfer by Esquivel & Raga (2013). We recommend the reader to read this paper and the earlier work by the UNAM team (Raga & Wang 1994; Raga et al. 1999) and by Raymond et al. (1988), which deal with the more complex shock geometries than the simple 1D plane parallel models presented here. A full treatment of time-dependent pre-ionisation in cases of complex geometry is beyond the scope of this paper.

5. APPLICATION TO HH34

The HH34 jet and its associated multiple bow shocks presents a particularly fine example with which to test our shock models. The inner jet, which emerges from the star HH34 IRS, has a series of multiple shocked knots along its length which all have a remarkably low excitation (Morse et al. 1993) and very large proper motions (Reipurth et al. 2002). The shocked knots are therefore internal to the jet, probably driven by velocity of mass ejection fluctuations in the outflow. In the IR, the jet displays very weak H_2 emission, but is very strong in [Fe II] (Stapelfeldt et al. 1991). The jet is likewise characterised by very strong [Fe II], [Ni II] and [Ca II] emissions in the optical, suggesting that it is both atomic and dust-free in nature (Morse et al. 1993; Reipurth & Bally 2001). The inner jet has already undergone detailed analysis in the paper by Hartigan et al. (1994), who demonstrated that the characteristic shock velocity is ~ 28 km/s, and that the ionisation fraction remains very low throughout the radiative shock structure. Based on an extensive grid of shock models, they derive both the mass loss rate and momentum flux in the jet.

The detailed structure in the HH34 jet has been revealed in the spectacular integral field study of Beck et al. (2007). They find the electron density as traced by the [S II]$\lambda\lambda$6731/6717 ratio peaks on the leading edge of each of the emission knots in the collimated jet, consistent with the compression and increase in ionisation caused by a shock. The density in each knot decreases systematically with distance from the central star, consistent with the expansion of the jet observed by Reipurth & Bally (2001). In addition, the radial velocity decreases with increasing distance from the central star, consistent with mass entrainment and the progressive dissipation of the mechanical energy flux of the jet through the action of internal working surface shocks along its length. A similar behaviour as been found in the HH111 jet by Cerqueira et al. (2015). Their high spatial resolution *Gemini MOS* IFU spectroscopy shows that the HH 111 jet has a fast, axial region with lower velocity shocks surrounded by a lower velocity sheath with higher velocity shocks.

The HH34 jet is merely the core of a much larger complex giant HH flow extending over 3pc (Devine et al. 1997). Some distance from the inner jet, the flow passes through a Mach disk structure, HH34, and this is enveloped in a higher-excitation bow shock, as seen clearly in the nice (colour) Hubble Space Telescope image of Reipurth et al. (2002). The counter-jet produces a similar structure HH34 N, which is followed further out by HH126, HH85 and HH33/40. On the jet side the corresponding regions are HH173, HH86, and HH87/88.

Optical spectrophotometry has been obtained by Morse et al. (1993) for both the Mach disk (HH34 MD),

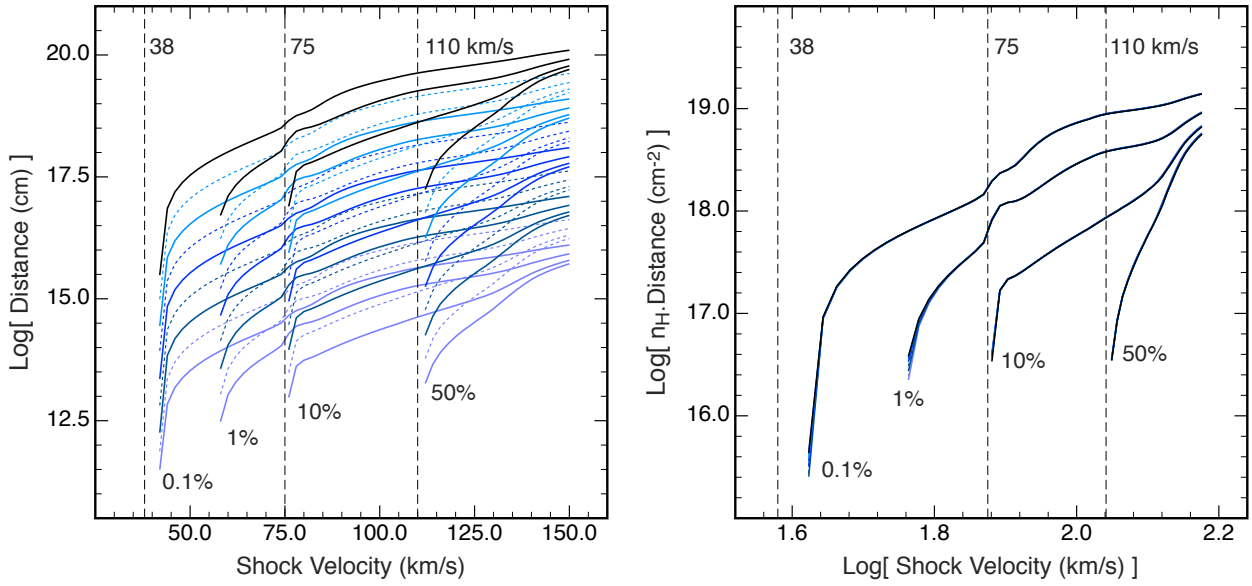

FIG. 11.— Left: The thickness of the precursor give at several limits to the pre-ionisation fraction as a function of both shock velocity and pre-shock density. The colour code for density is the same as in Figure 10. Right: The H column density to these same fractional ionisations. These curves are effectively independent of the pre-shock density.

and for the apex of the bow shock (HH34 apex) in HH34. However, a complete spectral separation between these two regions cannot be achieved as they are to a large degree co-spatial. Our shock modelling for these two regions will therefore use a linear sum of a lower velocity (Mach disk) shock, and a higher velocity (bow) shock emission.

5.1. *Modelling the HH34 jet*

In order to model the HH34 jet region, we note that the extremely high ratios of [O I] $\lambda\lambda 6300, 6363/H\alpha$ and [N I] $\lambda\lambda 5198, 5200/H\alpha$ imply a very low shock velocity in the range $22-30\,$km/s, as previously estimated by Hartigan et al. (1994). As noted above, in this velocity range the collisional excitation of the Balmer lines is a major contributor the the Balmer line flux, and the Balmer decrement is, by consequence, much steeper than that predicted in Case B. We therefore first estimate the shock velocity from the excitation (c.f. Figure 8), obtain the theoretical Balmer decrement appropriate to this velocity, and use this to determine the correct reddening correction for the Morse et al. (1993) data with the Blagrave et al. (2007) Orion region modified extinction law. From this, we determined a logarithmic reddening $c_{H\beta} = 0.2$ for the HH34 jet region. The de-reddened fluxes so obtained are given in Table 2. This same reddening correction was also applied to the two other regions of HH34, and the derived de-reddened fluxes are also given in the Table.

With the assumed abundance set, an extensive subgrid of 100 models was run over a restricted range of shock velocity ($22.5-27.5\,$km/s,and shock ram-pressure (corresponding to $n_{\rm H} = 4800 - 8000\,{\rm cm}^{-3}$ for a shock velocity of $25\,$km/s. These covered the vicinity of the best-fit solution.

In order to measure the goodness of fit of any particular model, we measure the degree to which it reproduces the density-sensitive [S II] $\lambda\lambda 6731/6717$ ratio, and we also seek to minimise the L1-norm for the fit. That is to say that we measure the modulus of the mean logarithmic difference in flux (relative to Hβ) between the model and the observations *viz.*;

$$\mathrm{L1} = \frac{1}{m}\sum_{n=1}^{m}\left|\log\left[\frac{F_n(\mathrm{model})}{F_n(\mathrm{obs.})}\right]\right|. \qquad (2)$$

This procedure weights fainter lines equally with stronger lines, and is therefore more sensitive to the values of the input parameters. We simultaneously fit at least 10 emission lines which are most sensitive to the shock velocity and ram pressure; effectively [O I], [O II] and if present, [O III] as well as the [N I], [N II], and [S II] lines. In addition, we fit the Balmer decrement Hα, Hβ and Hγ and estimate the heavy element abundances using the [Fe II] 5158Å [Ni II] 7378Å Mg I] 4561Å, Ca II 3933Å and [Ca II] 7291Å lines.

The fit so obtained is shown in Figure 12. The shock velocity is very tightly constrained by the line flux ratios, $v_s = 25.0 \pm 1.2\,$km/s, but the pre-shock density has a larger error which is set by the photometric error in the observations. We estimate the pre-shock hydrogen density to be $n_{\rm H} = 6800^{+3500}_{-2000}\,{\rm cm}^{-3}$.

In order to fit the lines of refractory elements, it is necessary to enhance the chemical abundances above the local concordance values. Indeed, all these elements, Mg, Ca, Fe and Ni must be enriched by approximately the same amount, $+0.22\,$dex, to obtain a satisfactory fit to the observations. The complete emission line predictions for our best-fit model ($v_s = 25\,$km/s, $n_{\rm H} = 6800\,{\rm cm}^{-3}$) is given in Table 2.

5.2. *HH34 Mach disk and Bowshock Regions*

As noted above, the Mach disk and the bowshock regions cannot be entirely separated in a spatial sense from

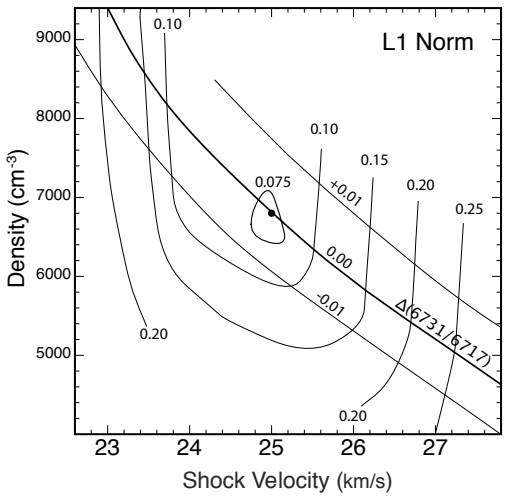

FIG. 12.— The goodness of fit contours for the HH34 jet region, derived from 100 shock models, plotted against the shock velocity and the pre-shock hydrogen density, $n_{\rm H}$. The L1-norm defines the shock velocity, $v_s = 25.0 \pm 1.2\,$km/s, while the density-sensitive [S II] $\lambda\lambda$6731/6717 ratio defines the pre-shock density, but with much larger error, set by the photometric error in the observations. We estimate $n_{\rm H} = 6800^{+3500}_{-2000}\,{\rm cm}^{-3}$.

one another. We have therefore adopted a model in which the observed spectrum results from a linear sum of a (high velocity) bow shock and a (lower velocity) cloud shock spectrum. To avoid introducing new variables, we adopt the chemical abundances determined for the HH43 jet. Since the ram pressure of the shock in the Mach disk drives the bowshock, the ram pressures in the two shocks are taken to be the same. The density in the Mach disk can be estimated from the density derived above for the HH34 jet, and from the ratio of the working surfaces of the Mach disk and the HH34jet shock. This ratio is derived from the HST images of Reipurth & Bally (2001) which show the jet to b 0.6 arcsec. in diameter (at bright knots I and J), while the [S II] - bright Mach disk area covers 10 arcsec. in diameter. The implied density of the Mach disk pre-shock region is $22^{+11}_{-7}\,{\rm cm}^{-3}$.

With this density, and matching the ram pressure in the Mach disk and bow shock, we varied the shock velocities, seeking to minimise the L1 norm in both regions. The bow shock has strong [O III], [O II] and [N II] emission relative to Hβ, but has weak [O I] and [N I], while most of the [O I] and [N I] emission arises in the Mach disk shock, so the contributions of the two can be readily separated. We find, for the Mach disk, $v_s = 34.0 \pm 2\,$km/s and $n_{\rm H} = 22^{+11}_{-7}\,{\rm cm}^{-3}$ while for the bow shock, $v_s = 80 \pm 10\,$km/s and $n_{\rm H} = 4^{+2}_{-1}\,{\rm cm}^{-3}$. In the observations of HH34 MD, the Mach disk shock contributes around 80% of the total Hβ emission, while the HH34 apex region has only a $\sim 30\%$ contribution. Again, as for the HH34 jet region, the refractory elements, Mg, Ca, Fe and Ni are enriched by 0.22 dex. The emission line fits are listed in Table 2.

5.3. *The physical parameters of HH34*

With the derived shock parameters, we can estimate a number of interesting parameters for the HH34 jet and for its Mach disk. Firstly, assuming that the jet is two-sided, we can estimate the mass-loss rate in the jet; $\dot{M} = (2\pi/4)\mu m_H D^2 v$ or

$$\dot{M} = 3{\times}10^{-8} \left[\frac{v}{250km\,s^{-1}}\right] \left[\frac{n_H}{10^4 cm^{-3}}\right] \left[\frac{D}{100AU}\right]^2 {\rm M}_\odot yr^{-1} \quad (3)$$

where n_H is the hydrogen particle density in the jet, v its velocity, and D its diameter. From Reipurth & Bally (2001) we have $D \sim 250\,$AU in the vicinity of the bright knots G,H and I. These authors estimate the space velocity of these knots to be $\sim 185\,$km/s. To this we must add the derived shock velocity to obtain the bulk velocity $v = 210\,$km/s. With our pre-shock density, $n_{\rm H} = 6800\,{\rm cm}^{-3}$, we have $\dot{M} = 1.1 \times 10^{-7}{\rm M}_\odot{\rm yr}^{-1}$. This compares well with the Hartigan et al. (1994) value of $1.5 \times 10^{-7}{\rm M}_\odot{\rm yr}^{-1}$, but is somewhat smaller than the value of $3.7 \times 10^{-7}{\rm M}_\odot{\rm yr}^{-1}$ derived by Bacciotti & Eislöffel (1999). The momentum flux (or thrust) of $\dot{M}v = 3.7 \times 10^{-5}{\rm M}_\odot\,{\rm km/s\,yr}^{-1}$, likewise similar to the $\dot{M}v = 4 \times 10^{-5}{\rm M}_\odot\,{\rm km/s\,yr}^{-1}$ derived by Hartigan et al. (1994), but again somewhat smaller than the Bacciotti & Eislöffel (1999) estimate; $\dot{M}v = 8.1{\times}10^{-5}{\rm M}_\odot\,{\rm km/s\,yr}^{-1}$. These differences are driven mainly by different author's estimates of the pre-shock density. For example, we derived $n_{\rm H} = 6800\,{\rm cm}^{-3}$, whereas Bacciotti & Eislöffel (1999) obtained $n_{\rm H} = 2 \times 10^4\,{\rm cm}^{-3}$ from their analysis. These differences are in turn driven by the estimated degree of pre-ionisation, and by the detailed structure of the radiative shock, both of which determine the measured electron density, which is the physical quantity that is used to estimate the pre-shock density.

The sideways expansion of the jet (assumed to be into a vacuum) is $v_{exp} = c_1\,[2/(\gamma-1)]^{1/2}$, where c_1 is the sound speed in the pre-shock gas, and $\gamma = 5/3$ is its adiabatic index. From the self-consistent pre-ionisation state computed in our model, we find a pre-shock temperature of $T = 280$K, corresponding to a sound speed of 0.5 km/s. Thus over the $\sim$ 200yr age of the jet (out to bright knots G,H and I) the jet would have expanded to a diameter of 140AU assuming thermal expansion acting alone. This is somewhat smaller than the observed diameter, 250AU. However, there is certainly some contribution to the transverse expansion due to post-shock turbulence in the jet. We must conclude that the jet was originally extremely well-collimated.

The enhanced abundances of the refractory elements tell us something about the launch region of the jet. It is clear that, not only must this lie within the grain sublimation radius, in order to return Ca, Fe and Mg to the gas phase, but also that the material being ejected has been chemically enhanced by having a greater fraction of its material derived from a dusty or rocky origin. Adopting a stellar luminosity ${\rm L}_* \sim 45{\rm L}_\odot$ (Cohen & Schwartz 1987), and assuming a grain sublimation temperature $T_{sub} \sim 1000$K, of we can estimate the grain sublimation radius; $r_{sub} = \left[{\rm L}_*/4\pi\sigma T_{sub}^4\right]$. Thus we can conclude that the jet is launched within a radius of 1.0 AU of the star, which is well within the zone of the rocky planets. If the (heavy element enhanced) material seen in the jet is of the same composition as the material currently accreting onto the star, then we can expect that the final photospheric abundances may be enhanced above the interstel-

TABLE 2
Best fit shock models for the three regions of HH34

Line ID and λ (Å):	HH34 jet [a]	Model[b c]	HH34 MD [a]	Model[b d]	HH34 apex [a]	Model[b e]
[O II] 3726,9	....	38.4	197.6	209.4	385.0	669.8
[Ne III] 3868	....	0.0	....	1.0	14.6	3.4
He I 3889, Hζ 3889	....			5.1	9.7	10.4
Ca II 3933	37.9	157.0	29.5	11.0	19.3	8.3
[Ne III] 3967, Ca II 3968, Hϵ 3970	37.8	86.7	25.2	11.2	26.4	12.7
[S II] 4069,76	106.2	96.3	21.9	11.8	15.3	8.2
Hδ 4101	14.5	12.0	18.6	11.3	24.6	16.0
[Fe II] 4244	39.0	46.9	4.1	5.8	4.5	2.9
[Fe II] 4277, 4287[f]	93.1	18.9	8.2	2.4	5.6	1.6
Hγ 4340, [Fe II] 4347	45.8	49.1	30.5	39.9	44.6	41.8
[O III] 4363,[Fe II] 4358	46.6	17.4	8.9	2.4	7.8	4.2
[Fe II] 4416	37.3	45.8	7.7	5.7	4.4	2.9
Mg I 4561,71	145.2	135.0	23.3	16.2	10.6	7.4
[Fe II] 4815	30.3	36.6	5.0	4.4	2.0	2.2
Hβ	100.0	100.0	100.0	100.0	100.0	100.0
[O III] 5007	....	0.0	13.7	13.7	52.3	47.1
[Fe II] 5158	152.1	167.2	18.1	20.7	6.7	10.4
[N I] 5198,5200	358.0	489.0	52.9	67.8	16.0	27.7
[Fe II] 5262,[Fe III]5270	72.9	94.4	7.5	14.7	4.7	16.3
[O I] 6300,64	1466.5	1543.0	158.0	192.3	70.7	75.4
Hα 6563	496.7	498.0	389.0	435.7	354.0	371.3
[N II] 6583	58.5	14.0	55.3	20.2	47.1	57.0
[S II] 6717	1649.9	1070.0	216.0	166.4	96.3	91.6
[S II] 6731	1441.6	932.0	149.1	115.4	66.5	65.1
[Fe II] 7155	200.5	....	10.0	....	3.9	....
[Ca II] 7291	478.2	342.0	65.5	30.1	22.1	20.2
[Ca II] 7324, [O II] 7325	179.1	248.0	40.2	30.6	27.3	49.3
[Ni II] 7378	240.2	169.1	10.6	6.1	4.5	5.0

[1] Reddening correction from Blagrave et al. (2007) Orion region modified extinction law with logarithmic reddening $c_{\mathrm{H}\beta} = 0.2$.
[2] Local galactic concordance abundance with Mg, Si, Ca, Fe and Ni enhanced by 0.22 dex.
[3] Shock velocity $v_s = 25\,\mathrm{km/s}$, preshock density $n_{\mathrm{H}} = 6800\,\mathrm{cm}^{-3}$
[4] 80% Mach disk: $v_s = 34\,\mathrm{km/s}$, $n_{\mathrm{H}} = 21.6\,\mathrm{cm}^{-3}$; 20%
Bow Shock: $v_s = 80\,\mathrm{km/s}$, $n_{\mathrm{H}} = 3.9\,\mathrm{cm}^{-3}$.
[5] 32% Mach disk: $v_s = 34\,\mathrm{km/s}$, $n_{\mathrm{H}} = 21.6\,\mathrm{cm}^{-3}$; 68%
Bow Shock: $v_s = 80\,\mathrm{km/s}$, $n_{\mathrm{H}} = 3.9\,\mathrm{cm}^{-3}$.
[5]Flux of [Fe II] λ4287 not predicted in MAPPINGS.

lar abundances from which the star originally formed.

The fact that the bow shock in HH34 has a shock velocity $\sim 80\,\mathrm{km/s}$, but a has proper motion and radial velocity consistent with a space velocity of $260 - 320\,\mathrm{km/s}$ (Devine et al. 1997; Reipurth et al. 2002) reveals that the substrate medium involved in the bow shock is already outflowing at a space velocity of $180 - 240\,\mathrm{km/s}$, and is therefore is part of the material ejected by HH34 IRS. This is consistent with the measured chemical abundances which are the same as in HH34 jet. We would expect that, as entrainment of the ambient ISM into this outflowing material becomes increasingly significant, the velocities of outflow in each of the HH complexes in the giant flow (on the north side HH34 N, HH126, HH85 and HH33/40, and on the south side, HH34, HH173, HH86, and HH87/88) will systematically decrease. This is consistent with the observed spatial velocities of these complexes which have been measured by Devine et al. (1997).

6. CONCLUSIONS

An understanding of the pre-ionisation conditions of low– and intermediate–velocity shocks is necessary for the proper interpretation spectra of HH Objects. In this paper, we have presented self-consistent models which permit us to estimate shock velocities, pre-shock densities and shock ram pressures using existing spectrophotometry. In particular we have applied these to a detailed modelling of the HH34 jet and Mach disk system, from which we have been able to derive physical parameters of the jet and outflow, and estimate the chemical abundances in this material. This study serves to show that shock modelling is vital if we are to understand the nature of outflows in pre-main sequence stellar systems, and the parameters derived for these outflows in turn informs studies aimed at understanding accretion and planetary system formation around these stars.

Currently, a major restriction to the application of this type of modelling is the fact that much of the spectrophotometry is old, does not cover the required wavelength range, is often taken with single-slit spectrographs at too low a spectral resolution, and has been de-reddened using inappropriate Balmer decrements. Therefore, more integral field spectroscopy such as has been obtained by Beck et al. (2007) and López et al. (2010) is sorely

needed. With such data, the 2D structure of the jet can be probed, and the different shock components (working surface shocks, Mach disk, bow shocks and cocoon shocks) can be separately analysed. For this purpose, the Wide Field Spectrograph (WiFeS) (Dopita et al. 2007) is ideally suited, since it can cover 3500–9500Å at a resolution of $R = 3000$ over a 38×25 arc sec. field. Studies of HH jets with this instrument are proceeding, and the analysis of this data will be the subject of future papers.

ACKNOWLEDGMENTS

We thank the referee for an expert review of our paper, which has helped us improve it by both adding essential material on the spatial scales of these shocks, and in clarifying the physics.. The authors acknowledges the support of the Australian Research Council (ARC) through Discovery project DP16010363.

REFERENCES

Allen, M. G., Groves, B. A., Dopita, M. A., Sutherland, R. S., & Kewley, L. J. 2008, ApJS, 178, 20
Bacciotti, F., & Eislöffel, J. 1999, A&A, 342, 717
Bally, J. 2009, Astrophysics and Space Science Proceedings, 13, 11
Bally, J., & Reipurth, B. 2001, ApJ, 546, 299
Bally, J., & Reipurth, B. 2002, in Revista Mexicana de Astronomia y Astrofisica, vol. 27, Vol. 13, Revista Mexicana de Astronomia y Astrofisica Conference Series, ed. W. J. Henney, W. Steffen, L. Binette, & A. Raga, 1–7
Bally, J., Reipurth, B., & Aspin, C. 2002a, ApJ, 574, L79
Bally, J., Reipurth, B., Walawender, J., & Armond, T. 2002b, AJ, 124, 2152
Beck, T. L., Riera, A., Raga, A. C., & Reipurth, B. 2007, AJ, 133, 1221
Beck-Winchatz, B., Bohm, K.-H., & Noriega-Crespo, A. 1996, AJ, 111, 346
Biro, S., & Raga, A. C. 1994, ApJ, 434, 221
Blagrave, K. P. M., Martin, P. G., Rubin, R. H., et al. 2007, ApJ, 655, 299
Bohm, K.-H., & Goodson, A. P. 1997, in IAU Symposium, Vol. 182, Herbig-Haro Flows and the Birth of Stars, ed. B. Reipurth & C. Bertout, 47–62
Böhm, K. H., Mannery, E., & Brugel, E. W. 1980, ApJ, 235, L137
Cerqueira, A. H., Vasconcelos, M. J., Raga, A. C., Feitosa, J., & Plana, H. 2015, AJ, 149, 98
Chevalier, R. A. 1978, Mem. Soc. Astron. Italiana, 49, 497
Cohen, M., & Schwartz, R. D. 1987, ApJ, 316, 311
Comerón, F., Pasquali, A., & Alves de Oliveira, C. 2013, A&A, 552, A30
Devine, D., Bally, J., Reipurth, B., & Heathcote, S. 1997, AJ, 114, 2095
Dopita, M., Hart, J., McGregor, P., et al. 2007, Ap&SS, 310, 255
Dopita, M. A. 1978, ApJS, 37, 117
Dopita, M. A., Binette, L., & Schwartz, R. D. 1982a, ApJ, 261, 183
Dopita, M. A., Caganoff, S., Schwartz, R. D., & Cohen, M. 1987, in IAU Symposium, Vol. 115, Star Forming Regions, ed. M. Peimbert & J. Jugaku, 346
Dopita, M. A., Evans, I., & Schwartz, R. D. 1982b, ApJ, 263, L73
Dopita, M. A., Seitenzahl, I. R., Sutherland, R. S., et al. 2016, ArXiv e-prints, arXiv:1605.02385
Dopita, M. A., & Sutherland, R. S. 1995, ApJ, 455, 468
—. 1996, ApJS, 102, 161
Edwards, S., Ray, T., & Mundt, R. 1993, in Protostars and Planets III, ed. E. H. Levy & J. I. Lunine, 567–602
Esquivel, A., & Raga, A. C. 2013, ApJ, 779, 111
Hartigan, P., Heathcote, S., Morse, J. A., Reipurth, B., & Bally, J. 2005, AJ, 130, 2197
Hartigan, P., Morse, J. A., & Raymond, J. 1994, ApJ, 436, 125
Hartigan, P., Raymond, J., & Hartmann, L. 1987, ApJ, 316, 323
Hartmann, L., & Raymond, J. C. 1984, ApJ, 276, 560
Heathcote, S., Reipurth, B., & Raga, A. C. 1998, AJ, 116, 1940
Henney, W. J. 1996, Rev. Mexicana Astron. Astrofis, 32
Kajdič, P., & Raga, A. C. 2007, ApJ, 670, 1173
Kim, J. S., Clarke, C. J., Fang, M., & Facchini, S. 2016, ApJ, 826, L15
López, R., García-Lorenzo, B., Sánchez, S. F., et al. 2010, MNRAS, 406, 2193
Morse, J. A., Heathcote, S., Hartigan, P., & Cecil, G. 1993, AJ, 106, 1139
Raga, A. C. 1995, in Revista Mexicana de Astronomia y Astrofisica, vol. 27, Vol. 1, Revista Mexicana de Astronomia y Astrofisica Conference Series, ed. S. Lizano & J. M. Torrelles, 103–117
Raga, A. C., & Bohm, K.-H. 1985, ApJS, 58, 201
Raga, A. C., Böhm, K.-H., & Cantó, J. 1996, Rev. Mexicana Astron. Astrofis, 32
Raga, A. C., Mellema, G., Arthur, S. J., et al. 1999, Rev. Mexicana Astron. Astrofis, 35, 123
Raga, A. C., Reipurth, B., Castellanos-Ramírez, A., Chiang, H.-F., & Bally, J. 2015, ApJ, 798, L1
Raga, A. C., Reipurth, B., Esquivel, A., & Bally, J. 2016, AJ, 151, 113
Raga, A. C., & Wang, L. 1994, MNRAS, 268, 354
Raymond, J. C., Hartmann, L., & Hartigan, P. 1988, ApJ, 326, 323
Reipurth, B., & Bally, J. 2001, ARA&A, 39, 403
Reipurth, B., & Cernicharo, J. 1995, in Revista Mexicana de Astronomia y Astrofisica, vol. 27, Vol. 1, Revista Mexicana de Astronomia y Astrofisica Conference Series, ed. S. Lizano & J. M. Torrelles, 43
Reipurth, B., & Heathcote, S. 1997, in IAU Symposium, Vol. 182, Herbig-Haro Flows and the Birth of Stars, ed. B. Reipurth & C. Bertout, 3–18
Reipurth, B., Heathcote, S., Morse, J., Hartigan, P., & Bally, J. 2002, AJ, 123, 362
Reipurth, B., Yu, K. C., Heathcote, S., Bally, J., & Rodríguez, L. F. 2000, AJ, 120, 1449
Riaz, B., & Whelan, E. T. 2015, ApJ, 815, L31
Schwartz, R. D. 1975, ApJ, 195, 631
—. 1983, ARA&A, 21, 209
Shull, J. M., & McKee, C. F. 1979, ApJ, 227, 131
Solf, J., Bohm, K. H., & Raga, A. 1988, ApJ, 334, 229
Stapelfeldt, K. R., Scoville, N. Z., Beichman, C. A., Hester, J. J., & Gautier, III, T. N. 1991, ApJ, 371, 226